AGU
ADVANCING EARTH AND SPACE SCIENCE

Geophysical Research Letters®

Key Points:
- The viscosity of peridotite melt has been measured down to lower-mantle conditions by in situ falling sphere viscometry
- Peridotite melt has a lower viscosity than expected from the viscosity of the endmembers
- The low viscosity of peridotite melt suggests a fractional solidification in the magma ocean, supporting a heterogeneous primitive mantle

Supporting Information:
Supporting Information may be found in the online version of this article.

Correspondence to:
L. Xie,
ddtuteng@gmail.com

Direct Viscosity Measurement of Peridotite Melt to Lower-Mantle Conditions: A Further Support for a Fractional Magma-Ocean Solidification at the Top of the Lower Mantle

Longjian Xie[1,2,3] [ID]**, Akira Yoneda[2,4], Tomoo Katsura[1]** [ID]**, Denis Andrault[5]** [ID]**, Yoshinori Tange[6]** [ID]**, and Yuji Higo[6]** [ID]

[1]Bayerisches Geoinstitut, University of Bayreuth, Bayreuth, Germany, [2]Institute for Planetary Materials, Okayama University, Tottori, Japan, [3]Now at Earth & Planets Laboratory, Carnegie Institute for Science, Washington, DC, USA, [4]Department of Earth and Space Science, Osaka University, Suita, Japan, [5]Laboratoire Magmas et Volcans, CNRS, IRD, OPGC, Université Clermont Auvergne, Clermont-Ferrand, France, [6]Japan Synchrotron Radiation Research Institute, Sayo, Japan

Abstract As evidenced by isotope geochemistry, the persistence of primitive reservoirs indicates that the earth's lower mantle is likely to be heterogeneous. Such heterogeneity could be a legacy from magma-ocean (MO) solidification. The viscosity of MO is a key parameter to constrain the solidification type of MO. Here we directly measure the viscosity of peridotite (an analog of MO composition) melt at the pressure-temperature conditions of the deep mantle, using the in situ falling sphere method. The viscosity of peridotite melt along liquidus is in the range of 38–17 mPa s at pressures from 7 to 25 GPa, which is 0.9–0.4 times of the estimation based on the viscosity of endmember compositions. Low viscosity favors fractional solidification and chemically layering of the early mantle at least to the top lower mantle, which could be a source of heterogeneity for the present mantle.

Plain Language Summary The earth experiences a large-scale melting and forms a deep magma ocean in its early history. The viscosity of peridotite melt is a key parameter for understanding the solidification type of magma ocean, which leads to the primitive mantle structure. This study directly measured the viscosity of peridotite melt to deep mantle conditions and revealed that peridotite melt has a lower value of viscosity than expected. The low viscosity of peridotite melt suggests a fractional solidification of the magma ocean, which supports a heterogeneous primitive mantle.

1. Introduction

Identifying the magma-ocean (MO) solidification type is vital to understand the evolution of the Earth's mantle leading to the present-day isotopic heterogeneity. The Earth is believed to have experienced large-scale melting owing to massive energy released during the accretion and differentiation, which formed MOs with various depths (e.g., Elkins-Tanton, 2012 and reference therein). The most important MO was caused by a giant Moon-forming impact (e.g., Tonks & Melosh, 1993), which may have reached the lower mantle's bottom. The solidification of this MO produced the initial mantle structure that evolved to the present-day mantle. If the solidification was fractional, the initial structure should already have had substantial chemical heterogeneity. If equilibrium solidification occurred, the present heterogeneity (e.g., Hofmann, 1997), which isotope geochemistry suggests, should have been produced later. Thus, an assumption of the solidification type leads to an entirely different scenario of mantle evolution. Based on phase relations and elemental partitioning at pressures less than 26 GPa, geochemical models showed that even ~10 wt% of bridgmanite segregation can substantially deviates the ratios of minor and trace elements from the observed ranges, suggesting a maximum fractionation of ~10 wt% (Ito et al., 2004; Liebske, Corgne, et al., 2005; Walter et al., 2004). However, no conclusion was made for the solidification type. Although the solidification type has been investigated by geodynamic modeling, poorly constrained physical parameters prevent the modeling from giving a definitive conclusion (Solomatov, 2007).

Although viscosity is an essential parameter for geodynamic modeling, the viscosity of peridotite melt has not been directly measured under lower-mantle conditions. It was measured at ambient pressure using a concentric cylinder viscometer (Dingwell et al., 2004) and at upper-mantle pressures up to 13 GPa using the in situ falling sphere viscometry in a multianvil apparatus (Liebske, Corgne, et al., 2005; Liebske, Schmickler, et al., 2005). Several studies measured melt viscosity with endmember compositions of peridotite, that is, forsterite, enstatite, and diopside, under conditions up to the top lower-mantle also by the falling sphere viscometry in a multianvil apparatus (Cochain et al., 2017; Reid et al., 2003; Xie et al., 2020). Although the combination of the logarithmic viscosity of endmember melt led to the peridotite-melt viscosity of 0.01–0.1 Pa s (Xie et al., 2020), this calculation should contain significant uncertainties due to the absence of a physically justified mixing law. The peridotite-melt viscosity was also estimated based on element diffusivity using the Eyring equation (Posner et al., 2018), but this estimation highly depends on the assumption of ionic translation distance. Although density function simulations also attempted to determine melt viscosity, investigations have been limited to simple endmember systems (Karki & Stixrude, 2010; Nevins et al., 2009; Verma & Karki, 2012).

In this study, we directly measured the peridotite-melt viscosity under top lower-mantle conditions, that is, pressures up to 25 GPa, by the in situ falling sphere viscometry in a multianvil apparatus to indicate a much lower viscosity than Xie et al.'s (2020) estimation by the combination of endmember viscosity. This low melt viscosity suggests a fractional solidification of the MO.

2. Methods

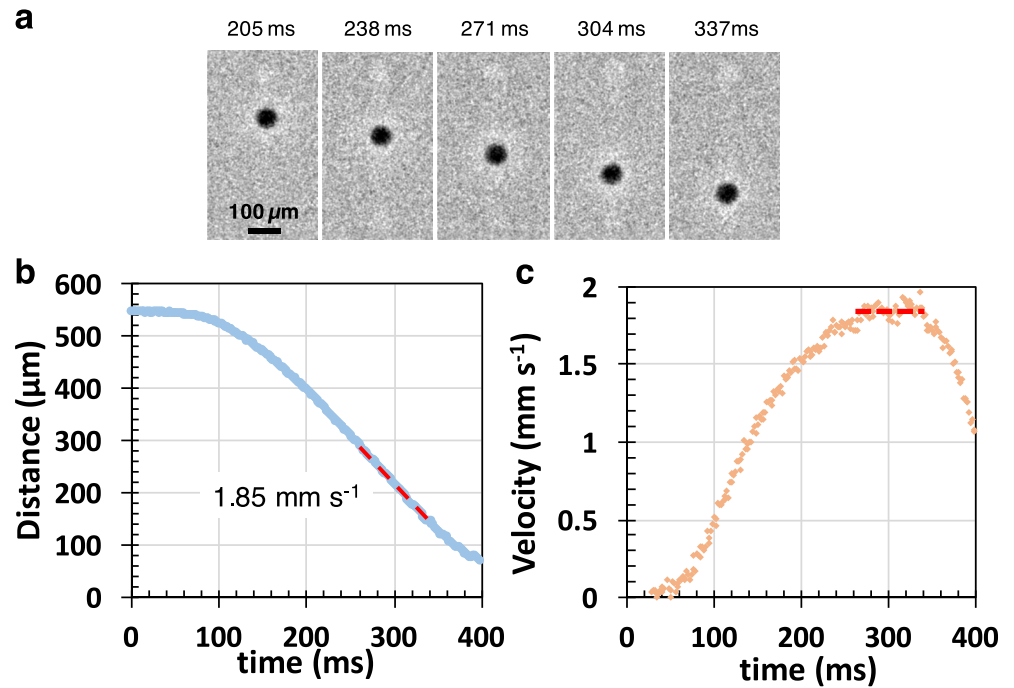### 2.1. Experiments at High Pressures and High Temperatures

The in situ falling sphere viscometry was performed in a double-stage 1,500 t multianvil apparatus (SPEED 1500) installed in the beamline BL04B1 at the synchrotron radiation facility SPring-8, Japan. Pressures were generated by WC cubes (carbide grade: TF05, Fujilloy, Japan) with 26 mm edge length and 4 mm truncation edge length. The cell assembly (Figure S1a) followed the design described in Xie et al. (2020). In order to melt the sample without sacrificing the quality of ultrafast radiography, we adopted X-ray transparent graphite and boron-doped diamond (BDD) heaters at pressures lower and higher than 8 GPa, respectively. The BDD heater especially renders it possible to generate temperatures up to 4,000 K (Xie et al., 2017), which is sufficient to melt peridotite completely at pressures up to 30 GPa. A peridotite sample with a Re sphere near the top as a probe was loaded in a graphite capsule. The Re-sphere diameter was as small as ~70 μm to induce a laminar flow around the falling spheres. Details of synthesizing sample and fabricating Re sphere are given in Text S1. A $W_{97}Re_3$-$W_{75}Re_{25}$ thermocouple was placed below the graphite capsule to monitor the power-temperature relationship before rapid heating for a sphere fall. A tube made of a mixture of MgO and 10 wt% diamond with ~1 μm grain size was placed outside the capsule to measure sample pressures based on the lattice constants of MgO with the equation of state proposed by Tange et al. (2009). The role of the diamond is to minimize grain growth of MgO and to obtain high-quality diffraction patterns.

After compression to a desired press load at room temperature, the temperature was slowly raised to 1,273 or 1,773 K to determine the sample pressure and power-temperature relationships, and then rapidly raised to a target temperature for the viscosity measurement. The target temperature was set 100–200 K above the liquidus temperature given by Zhang and Herzberg (1994). The temperature overshoot upon the rapid temperature increase was less than 200 K (Xie et al., 2020). The fall of the Re sphere was tracked by X-ray radiography using an ultra-fast camera with a maximum frame rate of 1,000 fps. The temperature difference is estimated ~60 K within the capsule. The pressure uncertainty was less than 1 GPa (Xie et al., 2020).

After the experiments, the texture and composition of the recovered samples were examined using a scanning electron microscope and an electron probe microanalyzer, respectively, at Bayerisches Geoinstitut, University of Bayreuth, Germany. The water content of Run S3301 was measured using Raman spectroscopy (Bolfan-Casanova et al., 2014) at Laboratoire Magmas et Volcans, France.

2.2. Viscosity Calculation and Error Analysis

The melt viscosity (η) was obtained from the terminal velocity based on Stokes' law:

Figure 1. Experimental observation of a falling sphere in Run S3299: (a) sequential radiographic images recorded during the fall of the Re-sphere, (b) position-time plot of the sphere. The sphere position was fitted by a Gaussian function in each X-ray radiographic image (blue symbols). The melt viscosity was calculated from the terminal velocity (dashed red line) using Equation 1. (c) Velocity-time plot of the sphere. The red dashed line is the best fit through the data points in the equilibrium regime.

$$\eta = \frac{2gr_s^2\left(\rho_s - \rho_m\right)W}{9v_s E} \tag{1}$$

$$W = 1 - 2.104\left(\frac{r_s}{r_c}\right) + 2.09\left(\frac{r_s}{r_c}\right)^3 - 0.95\left(\frac{r_s}{r_c}\right)^5 \tag{2}$$
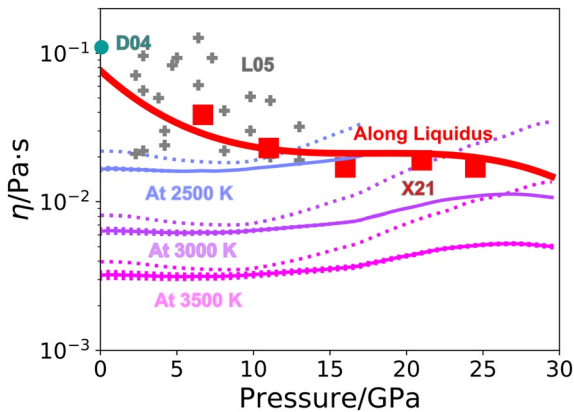
$$E = 1 + 3.3\left(\frac{r_s}{h_c}\right) \tag{3}$$

where v_s, r_s, ρ_s, ρ_m, and g are the terminal velocity, sphere radius, sphere density, melt density, and gravity acceleration, respectively. The parameters W and E are for correction due to the finite dimensions of the sample chamber with the radius r_c and height h_c (Faxén, 1922). The radius and density of the Re spheres were corrected using the EOS of Re (Zha et al., 2004). The density of peridotite melt was calculated from the liquid endmembers with forsterite, fayalite, enstatite, diopside, and anorthite compositions using the ideal mixing model (Thomas & Asimow, 2013 and ref. therein). The propagation of experimental uncertainties was evaluated using a Monte Carlo method (details in Xie et al., 2020). The reproducibility of this method was within 6%, according to Xie et al. (2020).

3. Results

3.1. Viscosity of Peridotite Melt Along Liquidus

Table S1 summarizes the experimental conditions and results. The viscosity was measured at temperatures slightly higher than the peridotite liquidus at pressures of 7, 11, 16, 21, and 25 GPa. An example of the Re-sphere trajectory is shown in Figure 1. The sphere reached a terminal velocity judging from the diagrams of the position and velocity versus time (Figures 1b and 1c). The recovered sample shows a reaction between the sphere and graphite capsule after the fall (Figure S1b), but we consider no reaction between the sphere

Figure 2. Viscosities of peridotite melt under pressure. The red squares denote the present experimental data, whose temperatures are just above the liquidus. The blue, purple, and magenta solid curves denote viscosities, which are calculated using parameterized Equation 4, at temperatures of 2,500, 3,000, 3,500 K, respectively. The dotted curves denote corresponding viscosities are calculated from the endmember viscosities. The red curve is the viscosity along the liquidus. D04: from Dingwell et al. (2004), L05: from Liebske, Schmickler, et al. (2005).

and melt during the sphere fall. The chemical composition of the melt after recovery is given in Table S2. The water content was under the detection limit (<100 ppm).

Figure 2 shows the viscosity of peridotite melt under pressure. Our results at pressures of 7 and 11 GPa fall in the range obtained by the previous high-pressure study (Liebske, Schmickler, et al., 2005). The much faster camera and smaller Re spheres than previously adopted enabled us to record much more images during the sphere fall and significantly improved the precision of viscosity measurements. The obtained viscosity decreases from 38 (2) mPa s at 7 GPa to 17 (1) mPa s at 16 GPa, slightly increases to 20 (1) mPa s at 20 GPa, and finally decreases to 17 (1) mPa s at 25 GPa. Such complex pressure dependences were also reported for the endmember viscosity by Xie et al. (2020).

3.2. Modeling Viscosity as a Function of Pressure and Temperature

We modeled peridotite viscosity as a function of pressure and temperature using the Arrhenius equation with normalization to the liquidus temperature based on the obtained data (for details of the method to resolve the *P-T* effects on viscosity, see Xie et al., 2020). The Arrhenius equation is therefore described as:

$$\eta(P,T) = \eta_0 \exp\left(\frac{H_a(P)}{kT}\right) = \eta_0 \exp\left(\frac{H_a^*(P)}{T^*(P)}\right) \tag{4}$$

where η_0, k, T, P, T_m, H_a, $T^*(P)$, and H_a^*, respectively, are the scale factor, the Boltzmann constant, the absolute temperature, the pressure, the liquidus temperature at a given pressure, the activation enthalpy, the dimensionless temperature $T/T_m(P)$, and the dimensionless activation enthalpy $H_a(P)/kT_m(P)$. Along the liquidus, $T^*(P)$ equals unity, and Equation 4 gives:

$$\ln(\eta) = \ln(\eta_0) + H_a^*(P) \tag{5}$$

We express $H_a^*(P)$ using a third-order polynomial based on our high-pressure and Dingwell et al.'s (2004) ambient-pressure viscosity data (Figure 2, Table S3). We noted that non-Arrhenian behavior was reported for a wide temperature range (from the glass transition to super liquidus temperatures) for peridotitic liquid (Dingwell et al., 2004; Liebske, Schmickler, et al., 2005). However, the temperature dependence of silicate melt viscosity over a limited temperature range can be reasonably well described by the Arrhenius equation (such as Ghosh & Karki, 2011; Reid et al., 2003; Urbain et al., 1982). In the present study, the important temperatures for discussing MO solidification are bounded to the range between the solidus and liquidus. We expect that viscosity is closely following the Arrhenian law in the present study.

We then calculated the viscosity along isotherms based on Equation 4 with the parameters shown in Table S3. The peridotite-melt viscosity shows a weak positive pressure dependence at constant temperatures in the investigated pressure range (Figure 2, solid curves). Considering the uncertainty of temperature, the peridotite-melt viscosity directly measured is comparable or slightly lower than (0.9–0.4 times of) that calculated from the endmember viscosity (dotted curves).

The pressure dependence of the melt viscosity along isotherms enables us to calculate the actual activation enthalpy and the activation volume. Even though the activation enthalpies of liquids from endmember to peridotitic composition show complex pressure dependences, a linear fitting can average the pressure dependence within 10% for each composition (Figure S3). We, therefore, estimated the viscosity beyond the experimental pressure range by linear extrapolation using fixed activation energy of 116 (1) kJ mol^{-1} and an activation volume of 0.63 (4) cm^3 mol^{-1} in the Arrhenius equation (Table 1).

Table 1
Model for the Activation Enthalpy (Figure S3)

Composition	η_0 (Pa s)	a (cm³ mol⁻¹)	b (kJ mol⁻¹)
Peridotite	$1.1\,(5) \times 10^{-4}$	0.63 (4)	116 (1)
Mg_2SiO_4 [a]	$2.3\,(12) \times 10^{-4}$	1.64 (7)	90 (1)
$MgSiO_3$ [a]	$8\,(5) \times 10^{-5}$	1.14 (19)	141 (3)
$CaMgSi_2O_6$ [a]	$3\,(7) \times 10^{-8}$	0.49 (16)	253 (3)

[a]Values according to Xie et al. (2020).

4. Discussion

4.1. Identification of Solidification Type of MO Based on the Obtained Viscosity Data

The ratio of grain size of minerals precipitating in the MO to the critical grain size, R_{mc}, is the crucial parameter to identify the MO solidification type of the Earth. If R_{mc} is larger than unity, the MO should be frozen by the fractional crystallization. If it is smaller, it should be by the equilibrium crystallization. We therefore evaluate the R_{mc} of the MO with various depths in this section. The critical grain size in the definition of R_{mc} is the maximum grain size with which the grain can be suspended in the convecting MO. Na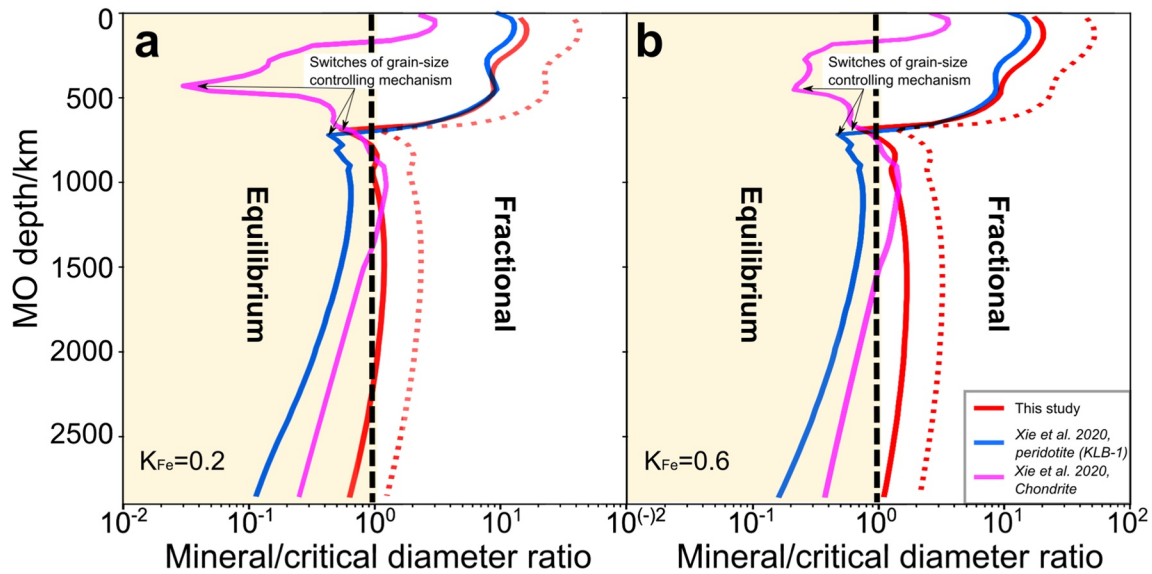mely, the negative buoyancy force acting on the grain is balanced with the viscous drag force by convecting magma so that the grain stays at the same depth in the upwelling (e.g., Solomatov, 2007) although grains should inevitably fall to the MO bottom in the downwelling. Assuming all the grains in the downwelling are entrained in the upwelling, we calculate the upper bound of critical grain size (the lower bound of R_{mc}) using the force balance between the negative buoyance and the viscous drag in the upwelling. The buoyancy force is the product of the gravity acceleration and the density difference between the mineral and melt. The viscous drag force is the product of the magma viscosity and the velocity of the grain relative to the convecting magma. The convection velocity is a function of the heat flux across the MO surface (Equation 9 in Text S2). Below, we briefly explain these parameters' evaluation, whose details are given in Text S2.

Among the above parameters, the surface heat flux, F_{sur}, is a function of T_{sur} by the thermal radiation to space. During the MO crystallization, a primordial atmosphere may have blanketed the thermal radiation. As shown in Text S3, we express this effect using the effective temperature (T_{eff}). The ratio of T_{eff} to T_{sur} is expressed using a parameter C_f. We obtain T_{sur} from the temperature at the MO bottom, T_{bot}, using the melting phase diagram of peridotite (Fiquet et al., 2010; Stixrude et al., 2009) along the adiabatic temperature gradient. For this calculation, the MO bottom is defined as the depth where the crystal fraction is 60%, denoted as D_{bot}, because the mineral-melt mixture changes its rheology from melt-like to solid-like across this crystal fraction (e.g., Lejeune & Richet, 1995). The cooling of the MO led to a decrease in T_{sur}, which decreased F_{sur} and T_{bot}, and made D_{bot} shallower.

The gain sizes of precipitating minerals should have been controlled by nucleation and growth by Ostwald ripening, respectively, when T_{sur} is higher and lower than the liquidus temperature of peridotite, T_{liq}, at the surface. When T_{sur} was higher than T_{liq} at the surface, the crystallization zone (CZ), defined as the region where minerals and melt coexist in MO, was extended from D_{bot} to the depth at which the liquidus and MO adiabatic intersect. Under this circumstance, all grains dissolved and disappeared near the surface in upwelling flow, and new grains nucleated at the CZ top in downwelling flow. This process limited the grain lifetime, which was about one week (Solomatov, 2007). Since this lifetime is too short for grain growth, nucleation should have controlled the grain size. When T_{sur} became lower than the T_{liq}, the CZ top reached the surface. Hence, some grains should have survived at the surface in upwelling flow, and the survived grains should have grown in downwelling flow. The growth of these grains should have continued until the MO completely solidified. Under this circumstance, the grain growth by Ostwald ripening should have controlled the grain size.

The adiabatic temperature gradient should significantly have affected the depth of the liquidus and MO adiabatic intersection, thus, in turn, the CZ thickness and the depth when the grain-size controlling mechanism switches. Unfortunately, the latent heat of crystallization of peridotite melt has only been measured up to 4 GPa (Kojitani & Akaogi, 1997). The latent heat causes a smaller temperature gradient, and therefore, a shallower depth of the intersection between the liquidus and the MO adiabatic than when neglecting the latent heat. As a result, the latent heat should have produced a thicker CZ. We considered two endmember cases: the CZ extends (1) in the entire MO or (2) up to the intersection between the liquidus and the adiabatic by neglecting the latent heat of crystallization. In case 1, Ostwald ripening increased the grain size from the onset of MO solidification, and the calculated *Rmc* represents an upper bound of the actual *Rmc*

Figure 3. Mineral/critical diameter ratio as a function of magma-ocean (MO) depth using bridgmanite as a solid phase and a solid-melt Fe partition coefficient of 0.2 (a) and 0.6 (b). Red solid and dotted curves are the ratios using the viscosity of peridotite melt from this study without a blanketing effect ($C_f = 1$) and with a 20% blanketing effect ($C_f = 0.8$), respectively. Light blue and purple lines are the ratios using the viscosity calculated from the endmembers for peridotite and chondrite compositions, respectively (Xie et al., 2020). The yellow (low Rmc) and white (high Rmc) regions indicate the chemical equilibrium and fractional solidifications, respectively. The black arrows mark the depth where the switch of grain-size controlling mechanism occurs.

in MO. In case 2, Ostwald ripening became significant after D_{bot} reaches 700 km, and the calculated Rmc represents a lower bound.

The density difference between the mineral and melt has some uncertainties due to insufficient knowledge about the Fe partition coefficient of the mineral to the melt (K_{Fe}). Here we assume that K_{Fe} is from 0.2 to 0.6 (Andrault et al., 2012). Figures S6b and S6c show the average mineral density and density difference with K_{Fe} of 0.2 and 0.6, respectively. With decreasing MO depth by the MO cooling, the density contrast should have first increased from 200 to 400 kg/m³ due to the higher bulk modulus of bridgmanite than the melt (Figure S6c). When the MO depth reached 900-km depth, it should have started to decrease to 100 kg/m³ because the first liquidus phase changed from bridgmanite to majorite at the MO top. It should have finally increased again to 300 kg/m³ due to the higher olivine bulk modulus than the melt. Thus, the density difference should have had a maximum and minimum when the MO bottom reached 900- and 400-km depths, respectively. The estimated density difference is 80 kg/m³ larger with $K_{Fe} = 0.6$ than $K_{Fe} = 0.6$ before the MO bottom reached 900-km depth, but nearly identical after that.

Based on the above scenario and estimation, we evaluate the average R_{mc} in the CZ as a function of the bottom depth of the cooling MO (Figure 3). When the MO bottom was located at depths from 2500 to 700 km, R_{mc} should have been slightly larger (up to a factor of ~1.5) than unity if $K_{Fe} = 0.2$ and no blanketing effect. If $K_{Fe} = 0.6$, the R_{mc} should have been up to 1.4 times larger than the case of $K_{Fe} = 0.2$, but this effect should have become negligibly small when the MO bottom became shallower than 700 km. If we consider the blanketing effect with $C_f = 0.8$, R_{mc} should have been twice larger. When the MO bottom reached 900 km depth, R_{mc} should have started to decrease so that it should have been less than unity when the MO bottom was at 700 km depth. With further decreasing the MO depth, R_{mc} should have rapidly increased and become larger than 10. Considering that viscosities at depths greater than 1,000 km contain significant uncertainties due to the far extrapolation of both pressure and temperature, we conclude that R_{mc} should have generally been greater than unity down to the top lower mantle, which supports the fractional crystallization in the MO, leading to chemical heterogeneity at least to the top lower mantle.

Our previous study (Xie et al., 2020) concluded that R_{mc} should have been less than unity in a peridotitic MO but larger than unity in a chondritic MO before the MO bottom had reached 700 km depth, if the blanketing effect is ignored. With a small blanketing effect ($C_f = 0.8$), R_{mc} should have been larger than unity in both

a peridotitic and chondritic MO at the top lower mantle. These previous results implied that the fractional solidification could occur at the top lower mantle in a peridotitic MO with the blanketing effect and a chondritic MO with any blanketing effect. Because the viscosity of peridotite melt in this study, especially under lower-mantle conditions, lower than that estimated using weighted sum endmember viscosities, we further confirm that the fractional solidification should have occurred down to the top lower mantle even in a peridotitic MO, in particular with some blanketing effects.

4.2. Origin of Lower-Mantle Heterogeneity

The present-day lower-mantle heterogeneity could arise from either (a) a heterogeneous primitive mantle or (b) later differentiation (such as partial melting) of a homogeneous primitive mantle. Since isotopic geochemistry such as noble-gas (Williams & Mukhopadhyay, 2019) and ^{182}W (Touboul et al., 2012) suggests mantle heterogeneities from early history (within ~100 Ma), it is likely that the primitive mantle was already heterogeneous. The present results suggest that the MO fractional crystallization should have formed a bridgmanite-enriched layer. The geodynamic simulation (Ballmer et al., 2017) demonstrated that the bridgmanite-enriched layer could have survived from mantle convection due to the high viscosity and been preserved to the present. Thus, the MO fractional crystallization suggested by the current study supports the chemical evolution model of the lower mantle explaining the primordial isotopic (noble-gas and ^{182}W) signatures surviving over geologic times and favors heterogeneous primitive mantle.

5. Conclusion

We investigated the viscosities of peridotite melt to lower-mantle conditions by in situ falling sphere viscometry using synchrotron radiation. We showed that the viscosity of peridotite melt is comparable or slightly lower (a factor of 0.9–0.4) than previously estimated based on the endmember viscosities. We applied the measured viscosity to model the MO solidification. The results further support the hypothesis of fractional solidification in the MO at least down to 1,000 km depths. The fractional solidification in the lower mantle should have induced the formation of a bridgmanite-enriched layer, which may have resisted mantle mixing by convection and contributed to the present-day lower-mantle heterogeneity.

Data Availability Statement

Data sets for this study (main paper and supporting information) are available at doi:10.5281/zenodo.5512934.

References

Andrault, D., Petitgirard, S., Lo Nigro, G., Devidal, J. L., Veronesi, G., Garbarino, G., & Mezouar, M. (2012). Solid-liquid iron partitioning in Earth's deep mantle. *Nature*, *487*(7407), 354–357. https://doi.org/10.1038/nature11294

Ballmer, M. D., Houser, C., Hernlund, J. W., Wentzcovitch, R. M., & Hirose, K. (2017). Persistence of strong silica-enriched domains in the Earth's lower mantle. *Nature Geoscience*, *10*(3), 236–240. https://doi.org/10.1038/ngeo2898

Bolfan-Casanova, N., Montagnac, G., & Reynard, B. (2014). Measurement of water contents in olivine using Raman spectroscopy. *American Mineralogist*, *99*(1), 149–156. https://doi.org/10.2138/am.2014.4444

Cochain, B., Sanloup, C., Leroy, C., & Kono, Y. (2017). Viscosity of mafic magmas at high pressures. *Geophysical Research Letters*, *44*(2), 818–826. https://doi.org/10.1002/2016GL071600

Dingwell, D. B., Courtial, P., Giordano, D., & Nichols, A. R. L. (2004). Viscosity of peridotite liquid. *Earth and Planetary Science Letters*, *226*(1–2), 127–138. https://doi.org/10.1016/j.epsl.2004.07.017

Elkins-Tanton, L. T. (2012). Magma oceans in the inner solar system. *Annual Review of Earth and Planetary Sciences*, *40*(1), 113–139. https://doi.org/10.1146/annurev-earth-042711-105503

Faxén, H. (1922). Der Widerstand gegen die Bewegung einer starren Kugel in einer zähen Flüssigkeit, die zwischen zwei parallelen ebenen Wänden eingeschlossen ist. *Annalen der Physik*, *373*(10), 89–119. https://doi.org/10.1002/andp.19223731003

Fiquet, G., Auzende, A. L., Siebert, J., Corgne, A., Bureau, H., Ozawa, H., & Garbarino, G. (2010). Melting of peridotite to 140 gigapascals. *Science*, *329*(5998), 1516–1518. https://doi.org/10.1126/science.1192448

Ghosh, D. B., & Karki, B. B. (2011). Diffusion and viscosity of Mg_2SiO_4 liquid at high pressure from first-principles simulations. *Geochimica et Cosmochimica Acta*, *75*(16), 4591–4600. https://doi.org/10.1016/j.gca.2011.05.030

Hofmann, A. W. (1997). Mantle geochemistry: The message from oceanic volcanism. *Nature*, *385*(6613), 218–229. https://doi.org/10.1038/385219a0

Ito, E., Kubo, A., Katsura, T., & Walter, M. J. (2004). Melting experiments of mantle materials under lower mantle conditions with implications for magma ocean differentiation. *Physics of the Earth and Planetary Interiors*, *143–144*, 397–406. https://doi.org/10.1016/j.pepi.2003.09.016

Karki, B. B., & Stixrude, L. P. (2010). Viscosity of MgSiO$_3$ liquid at earth's mantle conditions: Implications for an early magma ocean. *Science*, *328*(5979), 740–742. https://doi.org/10.1126/science.1188327

Kojitani, H., & Akaogi, M. (1997). Melting enthalpies of mantle peridotite: Calorimetric determinations in the system CaO-MgO-Al$_2$O$_3$-SiO$_2$ and application to magma generation. *Earth and Planetary Science Letters*, *153*(3–4), 209–222. https://doi.org/10.1016/s0012-821x(97)00186-6

Lejeune, A. M., & Richet, P. (1995). Rheology of crystal-bearing silicate melts: An experimental study at high viscosities. *Journal of Geophysical Research*, *100*(B3), 4215–4229. https://doi.org/10.1029/94JB02985

Liebske, C., Corgne, A., Frost, D. J., Rubie, D. C., & Wood, B. J. (2005). Compositional effects on element partitioning between Mg-silicate perovskite and silicate melts. *Contributions to Mineralogy and Petrology*, *149*(1), 113–128. https://doi.org/10.1007/s00410-004-0641-8

Liebske, C., Schmickler, B., Terasaki, H., Poe, B. T., Suzuki, A., Funakoshi, K., et al. (2005). Viscosity of peridotite liquid up to 13 GPa: Implications for magma ocean viscosities. *Earth and Planetary Science Letters*, *240*(3–4), 589–604. https://doi.org/10.1016/j.epsl.2005.10.004

Nevins, D., Spera, F. J., & Ghiorso, M. S. (2009). Shear viscosity and diffusion in liquid MgSiO$_3$: Transport properties and implications for terrestrial planet magma oceans. *American Mineralogist*, *94*(7), 975–980. https://doi.org/10.2138/am.2009.3092

Posner, E. S., Schmickler, B., & Rubie, D. C. (2018). Self-diffusion and chemical diffusion in peridotite melt at high pressure and implications for magma ocean viscosities. *Chemical Geology*, *502*, 66–75. https://doi.org/10.1016/j.chemgeo.2018.10.014

Reid, J. E., Suzuki, A., Funakoshi, K. I., Terasaki, H., Poe, B. T., Rubie, D. C., & Ohtani, E. (2003). The viscosity of CaMgSi2O6 liquid at pressures up to 13 GPa. *Physics of the Earth and Planetary Interiors*, *139*(1–2), 45–54. https://doi.org/10.1016/S0031-9201(03)00143-2

Solomatov, V. S. (2007). Magma oceans and primordial mantle differentiation. *Treatise on Geophysics*, *9*, 91–119. https://doi.org/10.1016/b978-044452748-6.00141-3

Stixrude, L., de Koker, N., Sun, N., Mookherjee, M., & Karki, B. B. (2009). Thermodynamics of silicate liquids in the deep Earth. *Earth and Planetary Science Letters*, *278*(3–4), 226–232. https://doi.org/10.1016/j.epsl.2008.12.006

Tange, Y., Nishihara, Y., & Tsuchiya, T. (2009). Unified analyses for P-V-T equation of state of MgO: A solution for pressure-scale problems in high P-T experiments. *Journal of Geophysical Research*, *114*(B3). https://doi.org/10.1029/2008JB005813

Thomas, C. W., & Asimow, P. D. (2013). Direct shock compression experiments on premolten forsterite and progress toward a consistent high-pressure equation of state for CaO-MgO-Al$_2$O$_3$-SiO$_2$-FeO liquids. *Journal of Geophysical Research: Solid Earth*, *118*(11), 5738–5752. https://doi.org/10.1002/jgrb.50374

Tonks, W. B., & Melosh, H. J. (1993). Magma ocean formation due to giant impacts. *Journal of Geophysical Research*, *98*(E3), 5319–5333. https://doi.org/10.1029/92JE02726

Touboul, M., Puchtel, I. S., & Walker, R. J. (2012). 182W evidence for long-term preservation of early mantle differentiation products. *Science*, *335*(6072), 1065–1069. https://doi.org/10.1126/science.1216351

Urbain, G., Bottinga, Y., & Richet, P. (1982). Viscosity of liquid silica, silicates and alumino-silicates. *Geochimica et Cosmochimica Acta*, *46*(6), 1061–1072. https://doi.org/10.1016/0016-7037(82)90059-X

Verma, A. K., & Karki, B. B. (2012). First-principles study of self-diffusion and viscous flow in diopside (CaMgSi$_2$O$_6$) liquid. *American Mineralogist*, *97*(11–12), 2049–2055. https://doi.org/10.2138/am.2012.4123

Walter, M. J., Nakamura, E., Trønnes, R. G., & Frost, D. J. (2004). Experimental constraints on crystallization differentiation in a deep magma ocean. *Geochimica et Cosmochimica Acta*, *68*(20), 4267–4284. https://doi.org/10.1016/j.gca.2004.03.014

Williams, C. D., & Mukhopadhyay, S. (2019). Capture of nebular gases during Earth's accretion is preserved in deep-mantle neon. *Nature*, *565*(7737), 78–81. https://doi.org/10.1038/s41586-018-0771-1

Xie, L., Yoneda, A., Yamazaki, D., Manthilake, G., Higo, Y., Tange, Y., et al. (2020). Formation of bridgmanite-enriched layer at the top lower-mantle during magma ocean solidification. *Nature Communications*, *11*(1). https://doi.org/10.1038/s41467-019-14071-8

Xie, L., Yoneda, A., Yoshino, T., Yamazaki, D., Tsujino, N., Higo, Y., et al. (2017). Synthesis of boron-doped diamond and its application as a heating material in a multi-anvil high-pressure apparatus. *Review of Scientific Instruments*, *88*(9), 093904. https://doi.org/10.1063/1.4993959

Zha, C. S., Bassett, W. A., & Shim, S. H. (2004). Rhenium, an in situ pressure calibrant for internally heated diamond anvil cells. *Review of Scientific Instruments*, *75*(7), 2409–2418. https://doi.org/10.1063/1.1765752

Zhang, J., & Herzberg, C. (1994). Melting experiments on anhydrous peridotite KLB-1. *Journal of Geophysical Research*, *99*, 17729–17742.